Supporting Information

Leveraging Sequential Doping of Semiconducting Polymers to Enable Functionally Graded Materials for Organic Thermoelectrics

Tengzhou Ma[1], Ban Xuan Dong[1], Garrett L. Grocke[1], Joseph Strzalka[2], Shrayesh N. Patel[1,3]*

[1]Pritzker School of Molecular Engineering, University of Chicago, Chicago, Illinois 60637, USA
[2]X-ray Science Division, [3]Center for Molecular Engineering, Argonne National Laboratory, Lemont, Illinois 60439, USA

Contents

1. Determination of doping level
2. GIWAXS data
   2.1. 2D images of Neat PBTTT
   2.2. 2D images collected on **NH** and **MH** segmented films
   2.3. Depth profiles of **L** and **H** segments
   2.4. Scattering profiles of **NH**, **LH** and **MH** segmented films
   2.5. Domain spacings at different positions on **NH** and **MH** segmented films
3. Raman data
   3.1. Raman mode assignments for neat and F4TCNQ vapor-doped PBTTT
   3.2. Raman maps of **L** and **H** segments with finer scale
   3.3. Raman maps of **NH** and **MH** segmented films
4. Conductivity and Seebeck data
   4.1. Seebeck coefficients measured using 3mm shadow mask
   4.2. Conductivity and Seebeck data of F4TCNQ-doped thiophene-based polymers
   4.3. Predicted Seebeck profiles across **NH**, **LH** and **MH** segmented films
5. Origin of the formation of interface region
6. Set-up and calibration for Seebeck measurements
7. Interdigitated electrode (IDE) fabrication
8. References

1. Determination of doping level

The doping level (MR), the molar ratio of F4TCNQ anion to PBTTT monomer repeat unit, was determined through Beer's law by using the absorption intensity of the F4TCNQ anion at 1.4 eV and the primary absorption peak of neat PBTTT at 2.3 eV. The absorption spectra of all doped samples were deconvoluted to the neutral, anion, and polaron components using the peak shape and relative intensities (Figure S1). Then, the dopant concentration (C_{F4^-}) was estimated using Beer's law with the F4TCNQ anion molar extinction coefficient ($\varepsilon \approx 50000$ L mol^{-1} cm^{-1})[1] and the underlying monomer concentration was estimated from PBTTT extinction coefficient at 2.3eV ($\varepsilon \approx 50000$ L mol^{-1} cm^{-1}).

PBTTT molar extinction coefficient calculation

Density of PBTTT is calculated from mass of repeat unit per unit cell. The unit cell volume of PBTTT, V_{uc}, is calculated as:

$$V_{uc} = abc\sqrt{1 - cos(\alpha)^2 - cos(\beta)^2 - cos(\gamma)^2 + 2 \cdot \cos(\alpha) \cdot \cos(\beta) \cdot \cos(\gamma)} = 1060\ \text{Å}^3$$

with the following parameters[2,3] : a = 21.5 Å, b = 5.4 Å, c = 13.5 Å, α = 137°, β = 86°, and γ = 89°.

Density of PBTTT, ρ_{PBTTT}, is then calculated as:

$$\rho_{PBTTT} = \frac{M_{BTTT} \times N_{ru}}{N_A \times V_{uc}} = \frac{694\ g \cdot mol^{-1}}{6.022 \times 10^{23} mol^{-1} \times 1060 \times 10^{-24}\ cm^3} \approx 1.1\ g \cdot cm^{-3}$$

where, M_{BTTT} is the molar mass of repeat unit, N_{ru} is the number of repeat units per unit cell (1 in the case of PBTTT) and N_A is the Avogadro constant.

With density of PBTTT as 1.1 g/cm^3, the molar concentration of PBTTT, C_{PBTTT}, is found to be:

$$C_{PBTTT} = \frac{\rho_{PBTTT}}{M_{BTTT}} = 1.58\ mol \cdot L^{-1}$$

Using Beer's law, the molar extinction coefficient of PBTTT at 2.3 eV is estimated as:

$$\varepsilon_{PBTTT} = \frac{A_{PBTTT}}{C_{PBTTT} \times L} \approx 50000\ L \cdot mol^{-1} \cdot cm^{-1}$$

where, A_{PBTTT} is the absorption of neat PBTTT at 2.3eV and L is the optical path length, in this case, the polymer film thickness (30 nm).

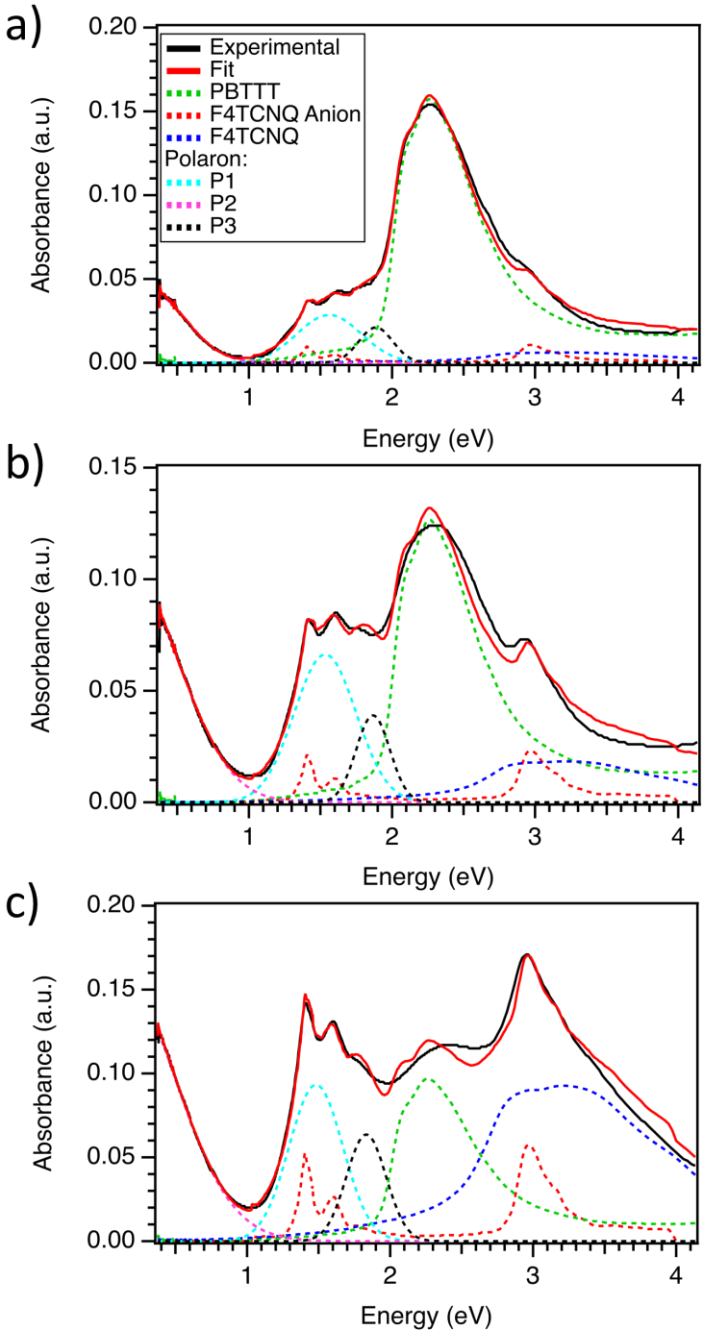

Figure S1. Absorption spectra fits for PBTTT thin films vapor-doped with F4TCNQ for various times. (a) 1.5 min = low (**L**), (b) 2 min = medium (**M**), and (c) 4 min = high (**H**)

2. GIWAXS data

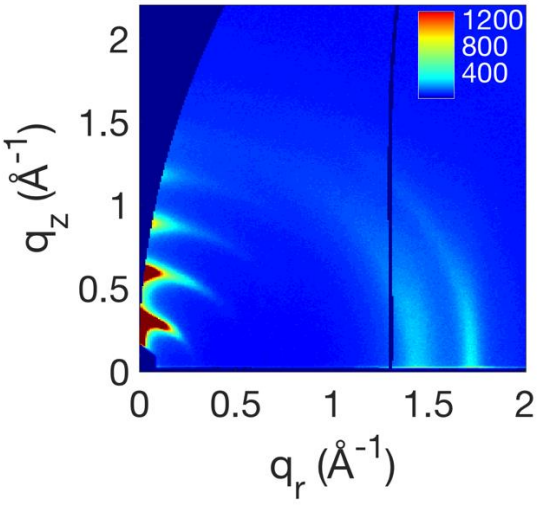

Figure S2. 2D GIWAXS image of neat PBTTT.

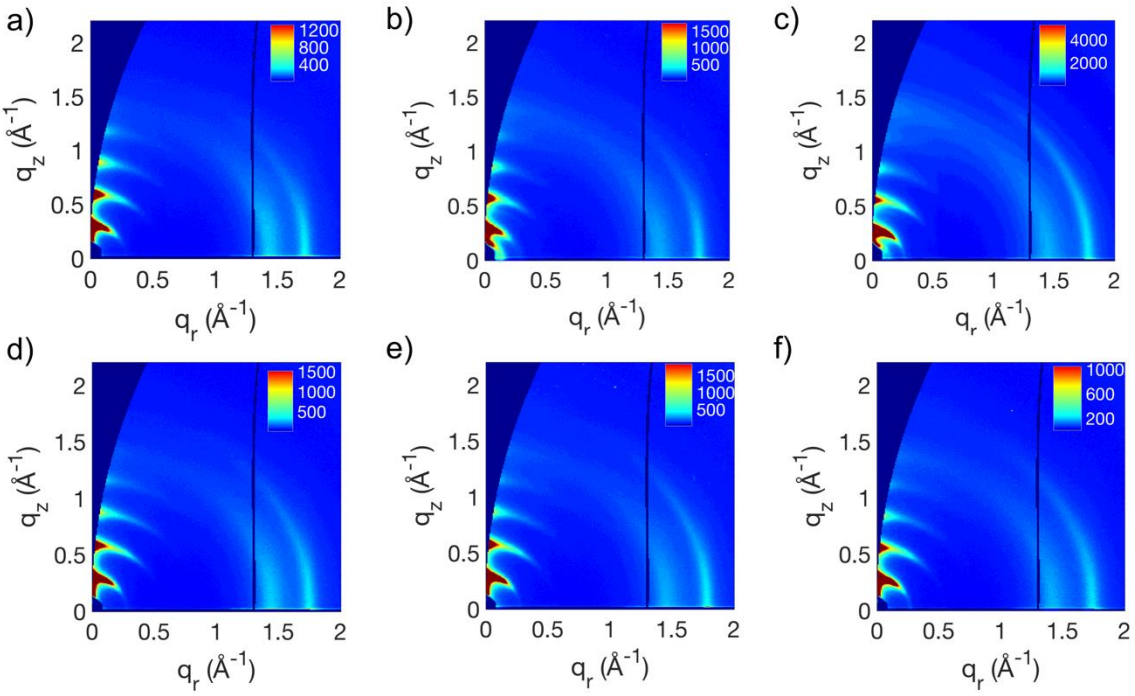

Figure S3. 2D GIWAXS images collected on **NH** segmented film at (a) **N** segment, (b) interface and (c) **H** segment, respectively. 2D GIWAXS images collected on **MH** segmented film at (d) **M** segment, (e) interface and (f) **H** segment, respectively.

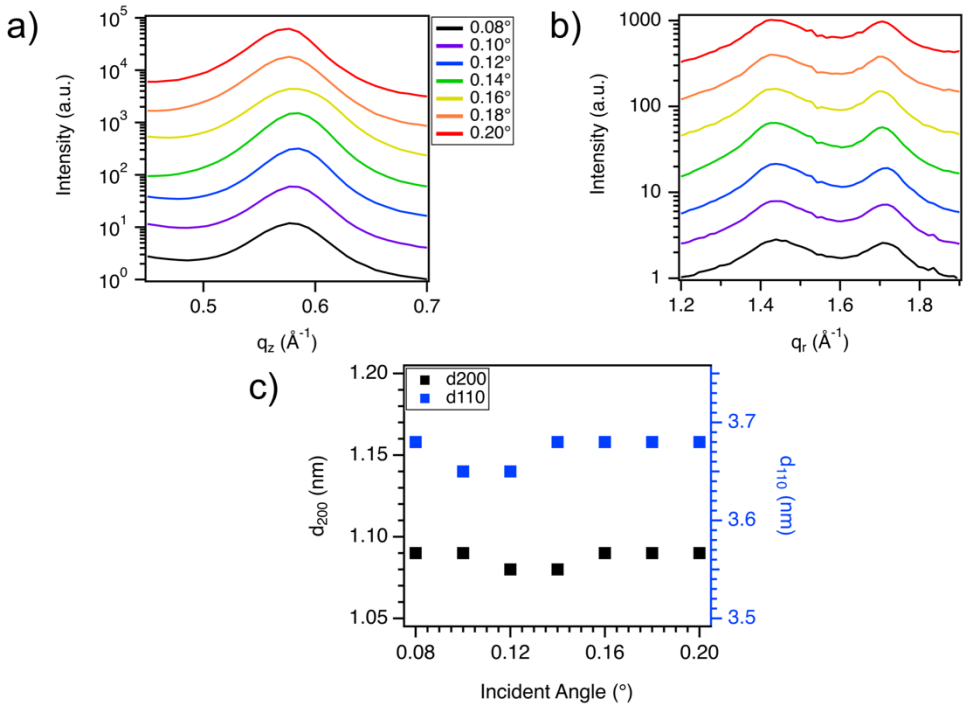

Figure S4. (a) Out-of-plane and (b) In-plane scattering profiles of a **L** segment at different incident angles; (c) Alkyl stacking spacing (d_{200}) and π-stacking spacing (d_{110}) at different incident angles. The critical angle of PBTTT is about 0.12°, and the critical angle of the Si substrate is about 0.166°. The scattering profiles have been vertically shifted for clarity. Note the difference in the scattering intensity is on the account of variation in scattering volume at different angle of incidence.

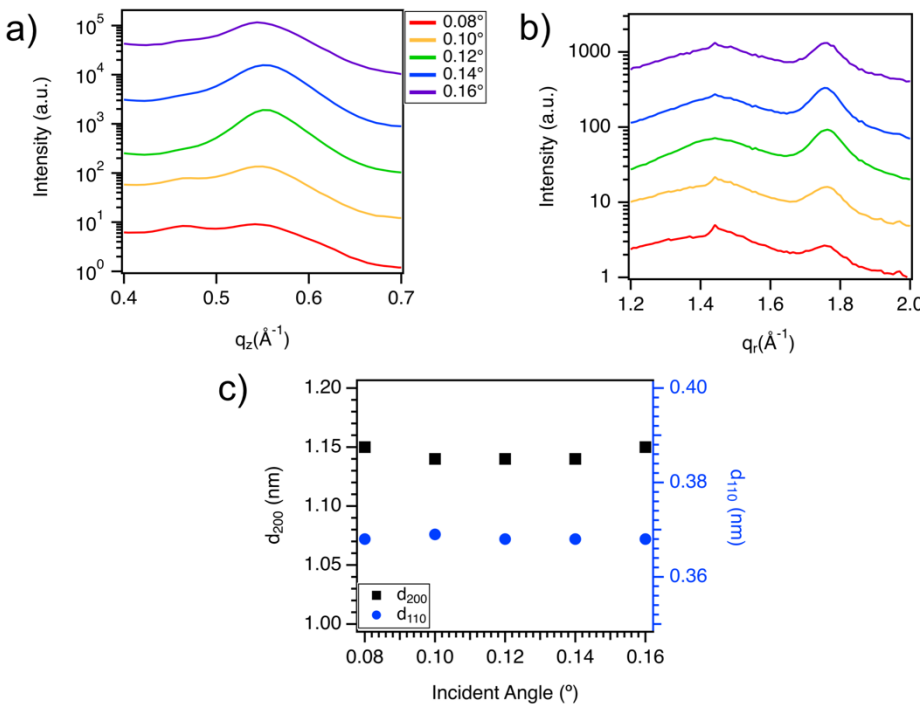

Figure S5. (a) Out-of-plane and (b) In-plane scattering profiles of a **H** segment at different incident angles; (c) Alkyl stacking spacing (d_{200}) and π-stacking spacing (d_{110}) at different incident angles. The critical angle of PBTTT is about 0.12°, and the critical angle of the Si substrate is about 0.166°. The scattering profiles have been vertically shifted for clarity. Note the difference in the scattering intensity is on the account of variation in scattering volume at different angle of incidence.

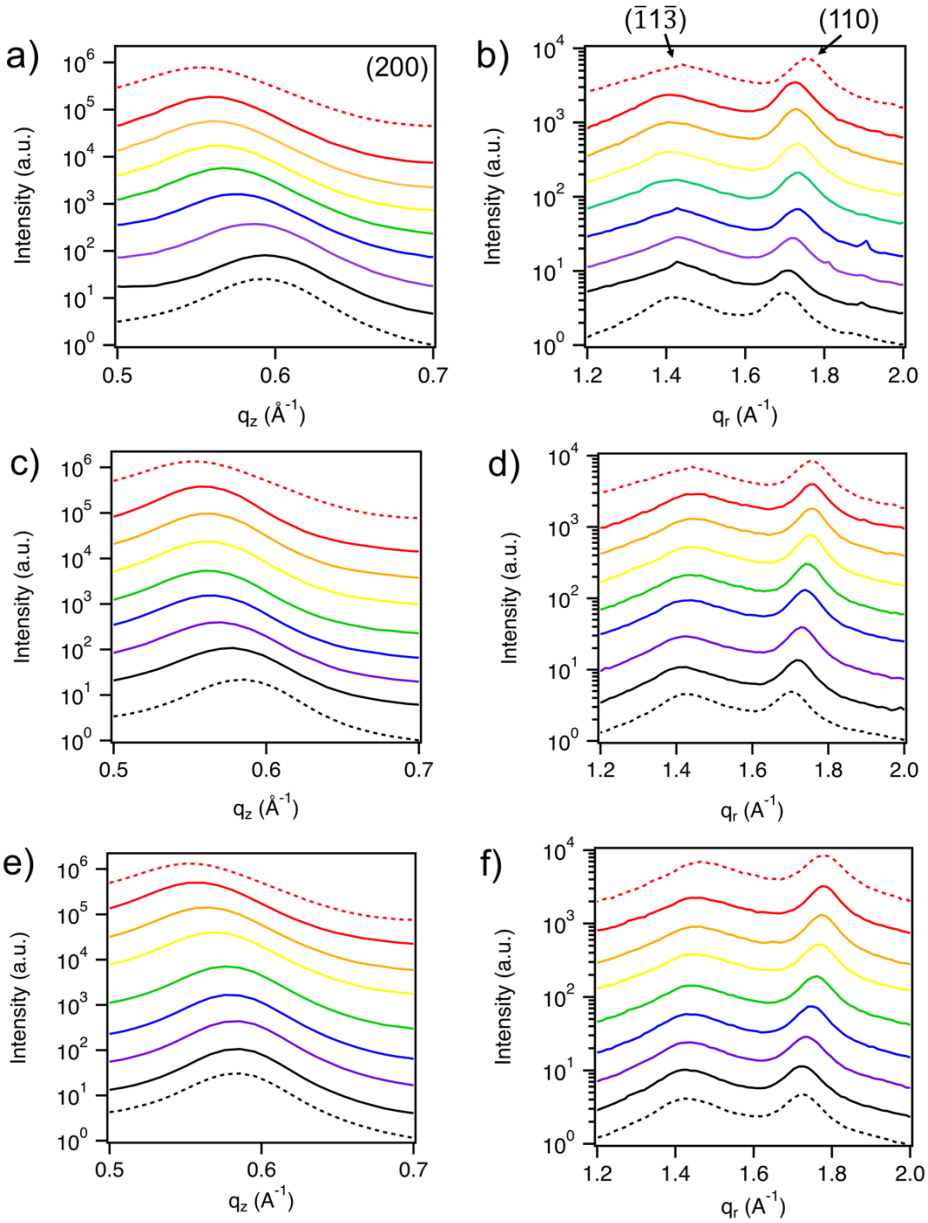

Figure S6. Out-of-plane (200) scattering peak profiles at different positions on (a) **NH**, (c) **LH** and (e) **MH** segmented films. In-plane scattering profiles for ($\bar{1}1\bar{3}$) and (110) at different positions on (b) **NH**, (d) **LH** and (f) **MH** segmented films. Dotted lines represent the measurements in the segments and solid lines represent the measurements across the interface.

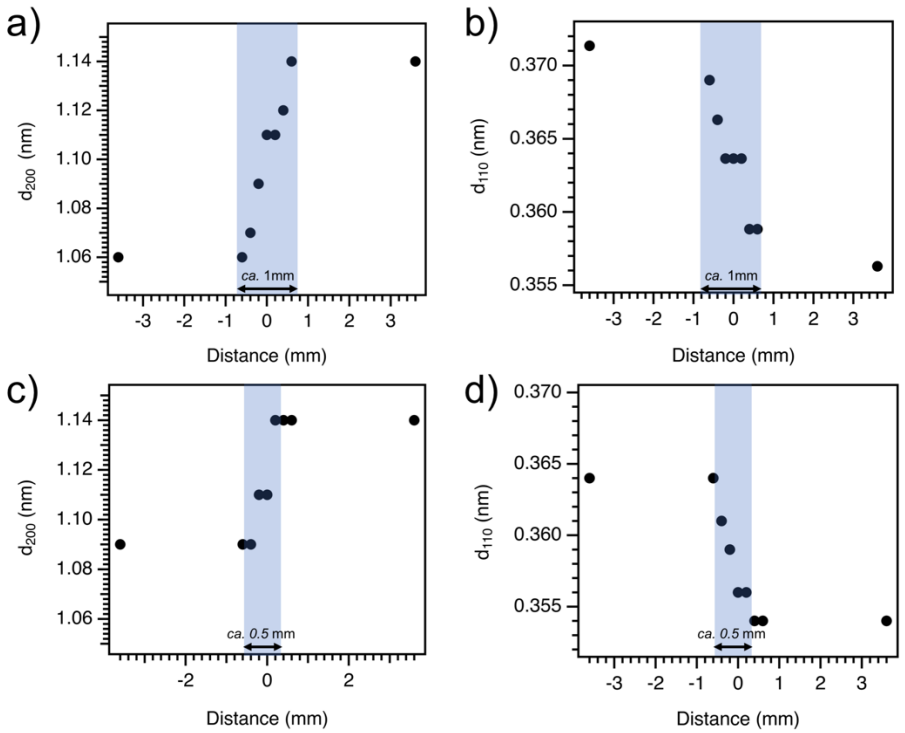

Figure S7. (a), (c) Alkyl stacking spacing (d_{200}) and (b), (d) π-stacking spacing (d_{110}) at different positions on **NH** and **MH** double-segmented PBTTT thin films obtained from GIWAXS.

3. Raman data

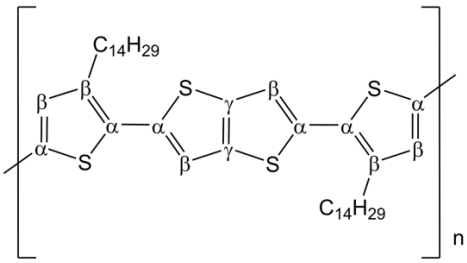

Figure S8. Chemical structure of PBTTT

Table S1. Raman mode assignment for neutral and F4TCNQ vapor-doped PBTTT

Mode	Wavenumber (cm^{-1})				Description[4]
	Neat	1.5min	2min	4min	
A	1394	1392	1391	1390	C_γ-C_γ intra-ring stretch
B	1415	1415	1413	1414	C_β-C_β intra-ring stretch
C	1461	1461	1461	1461	C_α-C_α inter-ring stretch
D	1490	1490	1489	1489	C_α-C_β intra-ring
E	N/A	N/A	1642	1642	F4TCNQ anion

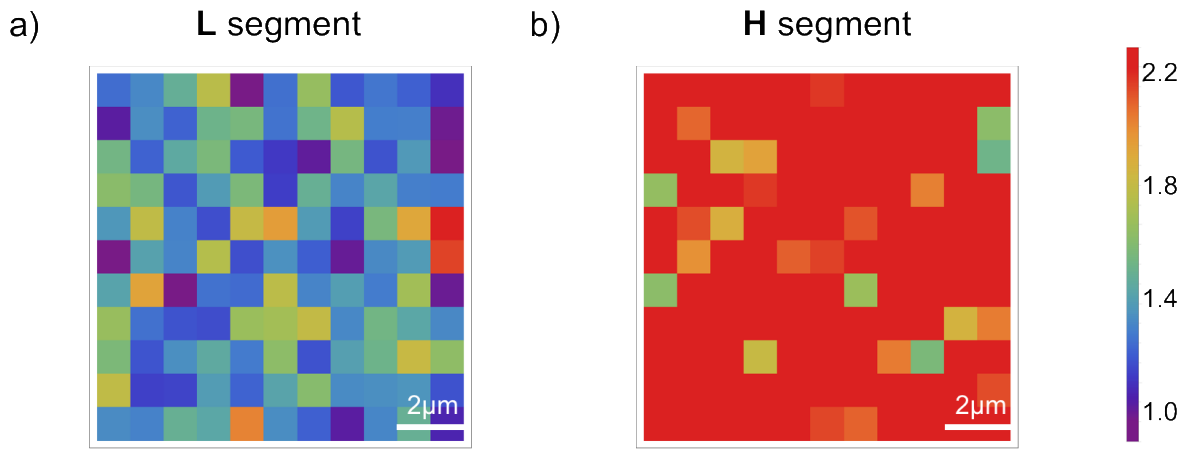

Figure S9. Raman maps with finer scale of peak height ratio of mode A/mode D on (a) **L** and (b) **H** segments.

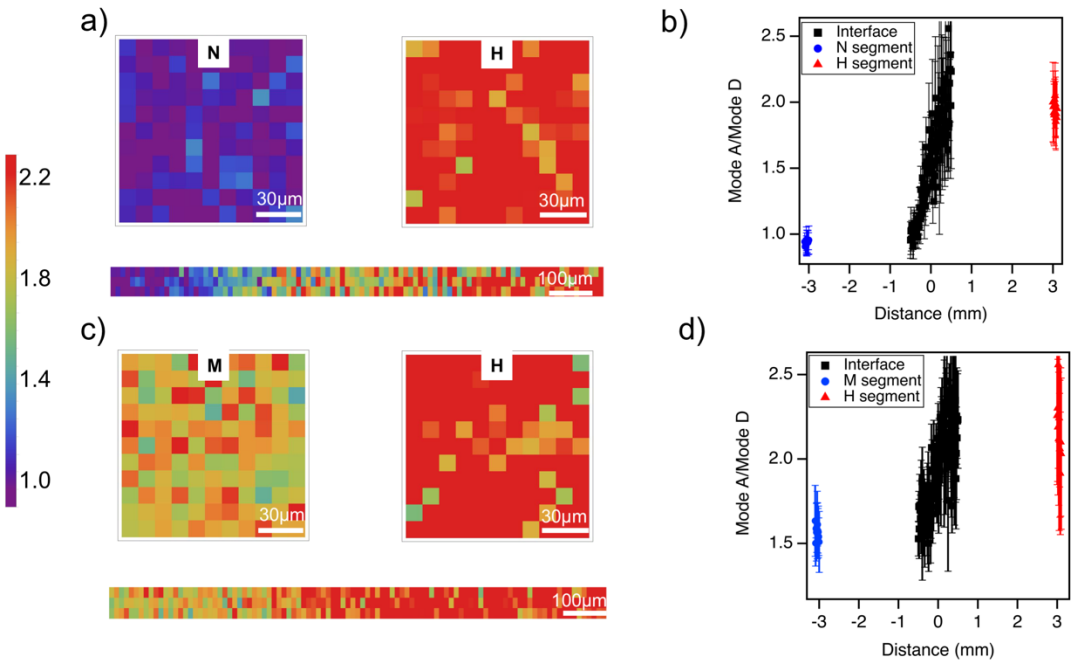

Figure S10. a) Raman maps of peak height ratio of mode A/mode D for a) NH and c) MH segmented films, respectively. Peak height ratio of mode A/mode D as a function of distance across b) NH and d) MH segmented films, respectively.

4. Conductivity and Seebeck data

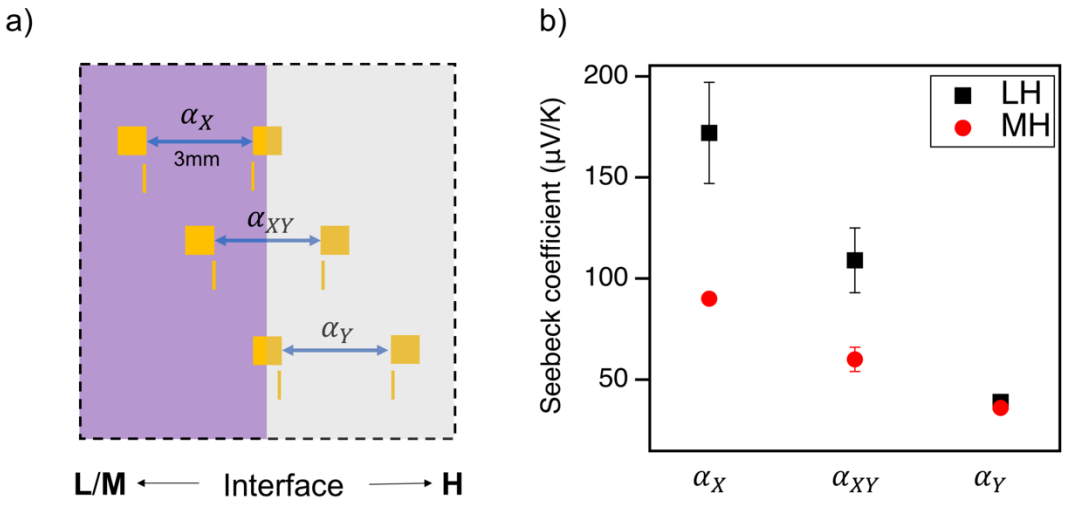

Figure S11. a) Schematic of contacts geometry for Seebeck measurements across 3 mm on **LH** and **MH** segmented films; b) Seebeck coefficient at different regions on **LH** and **MH** segmented films. (X = **L** or **M**; Y = **H**). **L**= low, **M**= medium, and **H**= high doping levels.

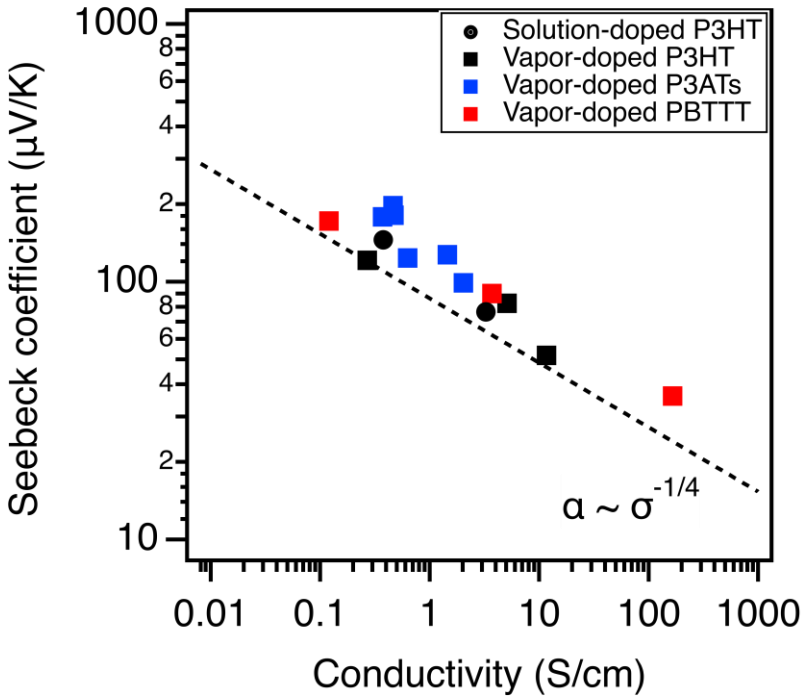

Figure S12. Seebeck coefficient as a function of electrical conductivity for F4TCNQ-doped polymers, P3HT (●,■), PBTTT (■) and P3BT, P3OT, P3DDT (■). The black dash line represents the empirical relationship of α proportional to $\sigma^{-1/4}$.

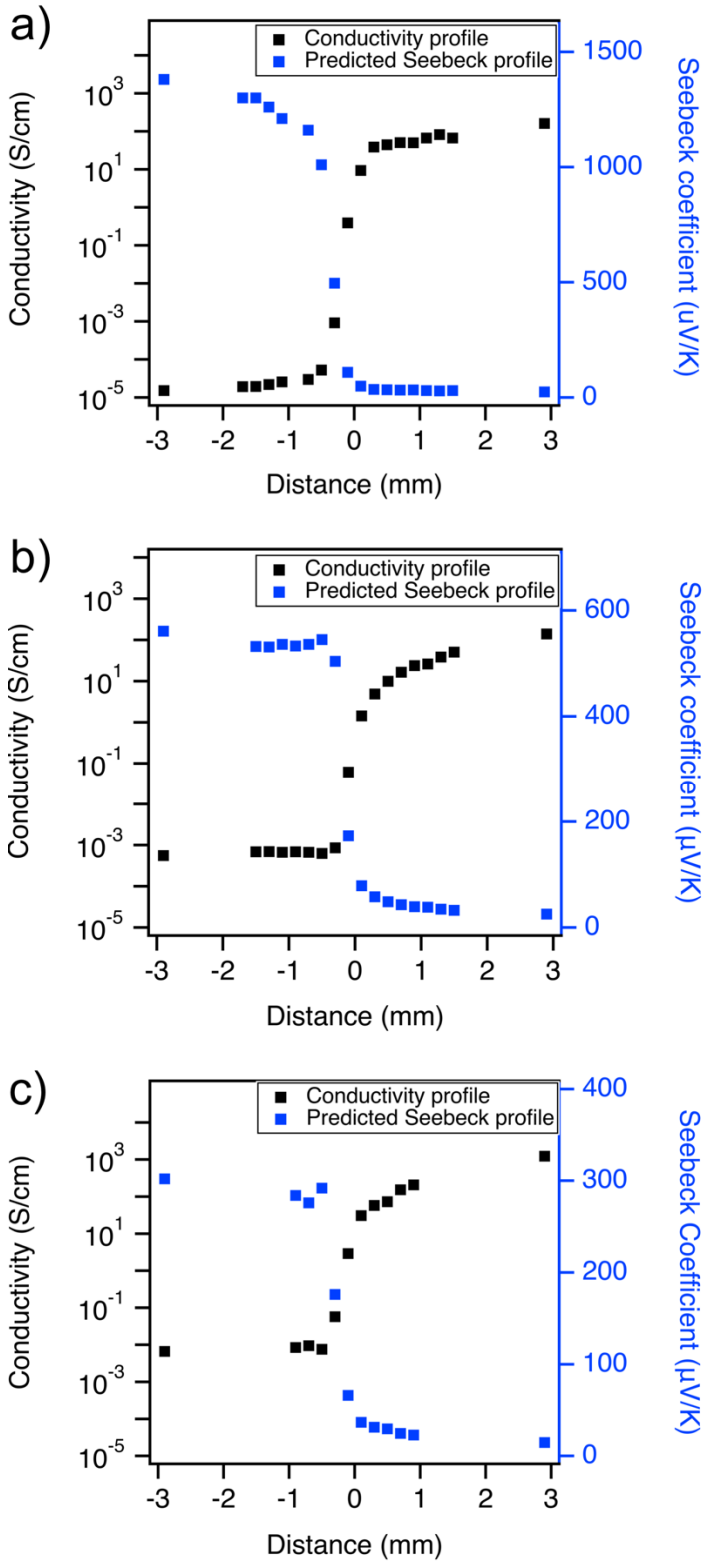

Figure S13. Predicted Seebeck profile across the (a) **NH**, (b) **LH** and (c) **MH** segmented films.

5. Origin of the formation of interface region

Since conductivity measurement, GIWAXS and Raman experiments all confirmed the existence of a diffuse interface region between the two segments of our samples, it is important to understand the origin of the formation of this interfacial region. One possible explanation is the diffusion of dopant/anion during vapor doping process or after the segmented film is established. While the specific diffusion coefficient of F4TCNQ in PBTTT has not been reported yet, the diffusion process of F4TCNQ in a similar thiophene-based polymer, P3HT upon thermal annealing has been studied[5]. Assuming that the diffusion coefficients of F4TCNQ dopant/anion in PBTTT is the same as in P3HT, we can estimate that the diffusion length of dopant/anion at 60°C (during vapor doping) or under room temperature (after establishing segmented film) lies in the micrometer scale which is much lower than the observed width of the interfacial region in our study. Therefore, the formation of this interface is unlikely due to dopant or anion diffusion. We thus attribute the origin of the formation of the interface region to our specific fabrication process. In our experiments, the Teflon mask (**Figure S14**) was placed slightly above the polymer surface to avoid scratches on the film. We suspect that this minor gap between the bar and polymer allowed a small amount of dopant vapor to diffuse underneath the bar, leading to the formation of the diffuse interface. This also explains why the interface regions are narrower in **LH** and **MH** segmented films as the time for dopant vapor diffusion is shorter.

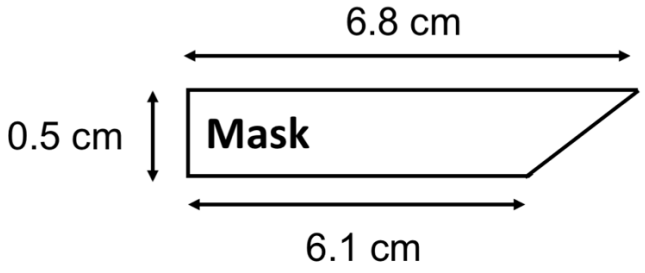

Figure S14. Schematic of the Teflon mask used in fabrication of double – segmented thin films.

6. Set-up and calibration for Seebeck measurements

Figure S15 shows the customized setup of the Seebeck coefficient measurement. Two peltier elements were placed 5 mm apart to provide the temperature difference ($\Delta T = T_H - T_C$). Gold contact pads 1 mm or 3 mm apart were evaporated onto the sample. The sample was placed in a way where the midpoint between gold pads was approximately the midline of the gap between the Peltier elements.

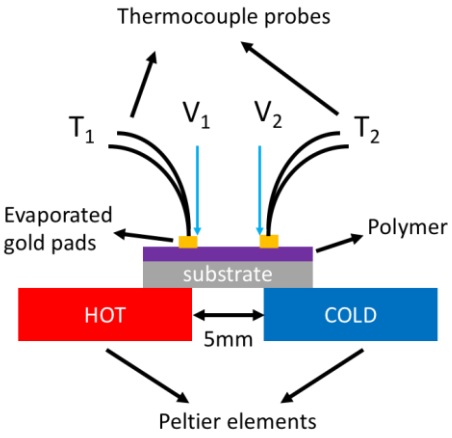

Figure S15. Schematic of Seebeck measurement setup.

The thermocouples for temperature measurements and the tungsten tips for voltage measurements were aligned at the same vertical position when we did our Seebeck measurements. The thermocouple tip was placed at the edge of the gold pad, which was in vertical alignment with the strip for the voltage probe. This setup would allow the distance between the thermocouple probes to be the same as distance between voltage tips in all of the measurements, which ensures proper Seebeck measurements. A minimal amount of thermal conductive silicon paste was applied to the thermocouple beads to ensure good thermal contact between the thermocouple and the sample. The Peltier elements were connected to make one side hot and one side cold when +1V was

applied and reverse the temperature gradient was achieved under –1V. There was a 200s settling time to reach the steady-state temperature and voltage gradient. At each temperature gradient, five consecutive measurements were taken 1 s apart. A typical Seebeck measurement scan is shown in **Figure S16**. For each sample, both forward and reverse scan were carried out to obtain an average Seebeck value.

Calibration measurements were carried out on multiple Nickel (>99.9%) samples from the same foil (**Figure S17**). After subtracting Seebeck coefficient of gold at 25°C (+1.94 μV/K)[6] , the average Seebeck coefficient of Ni was calculated to be –20.3 ± 1.3 μV/K, which matched well with previous literatures (–19 μV/K at 25°C) [7–9]. The systematic error was estimated from the standard deviation of the measurements, which is approximately 10%. Seebeck coefficients of F4TCNQ-doped thiophene based polymers were measured using our Seebeck set-up (**Figure S12**). The dash line is an empirical relation between α and σ, which obeys a power law as α proportional to $\sigma^{-1/4}$ and matches with previous study on transport properties[10].

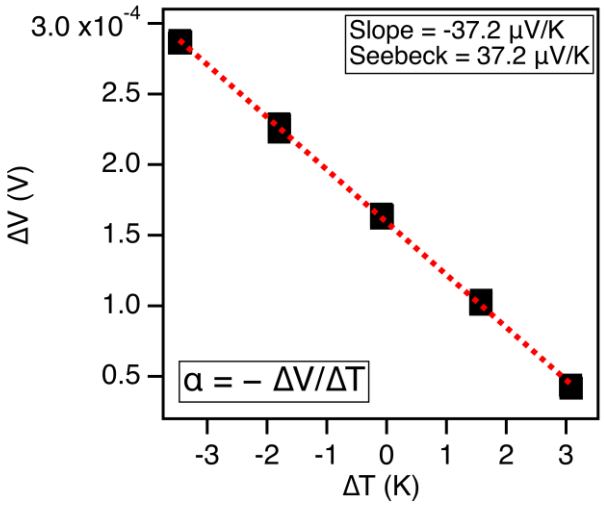

Figure S16. Typical Seebeck coefficient measurement curve (4 min doped PBTTT). Seebeck coefficient is the negative of the slope from the linear fit through the (ΔT, ΔV) points. 5 measurements for each steady-state ΔT are recorded.

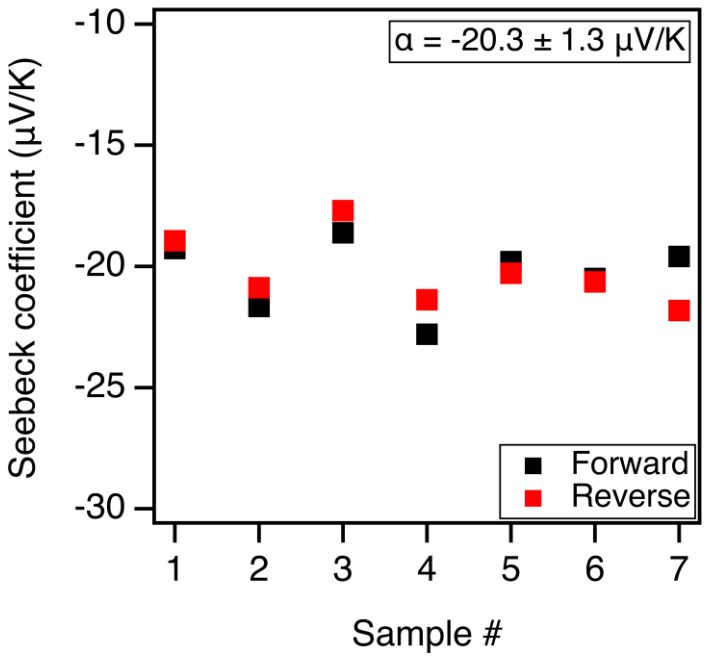

Figure S17. Seebeck coefficients of Nickel measured at 25°C.

7. Interdigitated electrode (IDE) fabrication

Si wafers with 1 μm of thermal oxide were first cleaned with a 300W oxygen plasma. A monolayer of hexamethyldisilazane (HMDS) is then deposited on the wafer in a vacuum oven at 110 °C under N_2 flow to promote photoresist adhesion. AZ nlof 2020 negative photoresist was spun cast at 3500 rpm for 45 seconds onto the wafer. IDE pattern was written with a Heidelberg MLA150 Direct Write Lithographer and AZ 300 MIF developer (tetramethylammonium hydroxide in water) was used to remove the patterned areas of the photoresist. E-beam evaporation of 5 nm titanium followed by 95 nm of gold was then applied to create the electrodes using an Angstrom EvoVac electron-beam evaporator. Liftoff of the excess metal and removal of the remaining photoresist was achieved by soaking the wafer in an 80 °C bath of n-methyl-2-pyyrolidone (NMP) overnight followed by sonication in fresh NMP. Wafers were subsequently rinsed with acetone, IPA, and deionized water. A single 4" wafer contains as many as 24 IDE devices. The work flow for fabrication of the IDEs is shown in **Figure S18**.

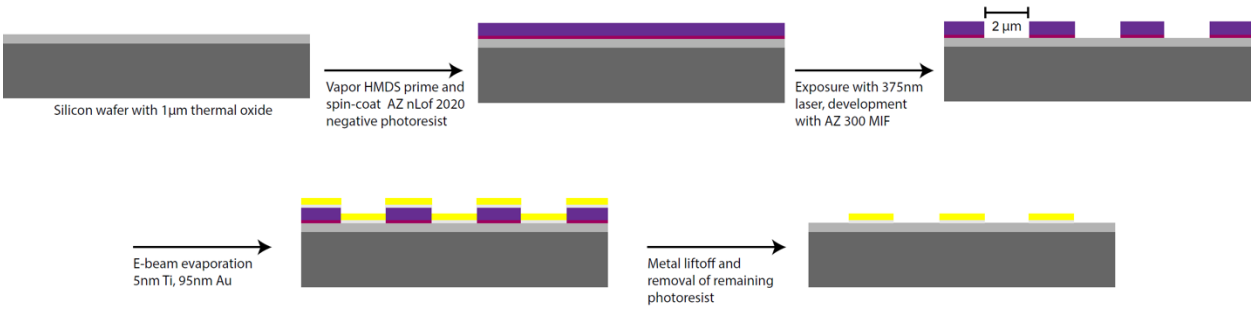

Figure S18. Work flow for fabrication of micron sized IDEs.

8. References

(1) Dixon, D. A.; Calabrese, J. C.; Miller, J. S. Crystal and Molecular Structure of the 2:1 Charge-Transfer Salt of Decamethylferrocene and Perfluoro-7,7,8,8-Tetracyano-p-Quinodimethane: [[Fe(C5Me5)2]+.Cntdot.]2[TCNQF4]2-. The Electronic Structure of [TCNQF4]n (n = 0, 1-, 2-). *J. Phys. Chem.* **1989**, *93* (6), 2284–2291.

(2) Cho, E.; Risko, C.; Kim, D.; Gysel, R.; Cates Miller, N.; Breiby, D. W.; McGehee, M. D.; Toney, M. F.; Kline, R. J.; Bredas, J. L. Three-Dimensional Packing Structure and Electronic Properties of Biaxially Oriented Poly(2,5-Bis(3-Alkylthiophene-2-Yl)Thieno[3,2- b]Thiophene) Films. *J. Am. Chem. Soc.* **2012**, *134* (14), 6177–6190.

(3) Brocorens, P.; Van Vooren, A.; Chabinyc, M. L.; Toney, M. F.; Shkunov, M.; Heeney, M.; McCulloch, I.; Cornil, J.; Lazzaroni, R. Solid-State Supramolecular Organization of Polythiophene Chains Containing Thienothiophene Units. *Adv. Mater.* **2009**, *21* (10-11), 1193–1198.

(4) Fujimoto, R.; Yamashita, Y.; Kumagai, S.; Tsurumi, J.; Hinderhofer, A.; Broch, K.; Schreiber, F.; Watanabe, S.; Takeya, J. Molecular Doping in Organic Semiconductors: Fully Solution-Processed, Vacuum-Free Doping with Metal-Organic Complexes in an Orthogonal Solvent. *J. Mater. Chem. C* **2017**, *5* (46), 12023–12030.

(5) Li, J.; Koshnick, C.; Diallo, S. O.; Ackling, S.; Huang, D. M.; Jacobs, I. E.; Harrelson, T. F.; Hong, K.; Zhang, G.; Beckett, J.; et al. Quantitative Measurements of the Temperature-Dependent Microscopic and Macroscopic Dynamics of a Molecular Dopant in a Conjugated Polymer. *Macromolecules* **2017**, *50* (14), 5476–5489.

(6) Bubnova, O.; Khan, Z. U.; Malti, A.; Braun, S.; Fahlman, M.; Berggren, M.; Crispin, X. Optimization of the Thermoelectric Figure of Merit in the Conducting Polymer Poly(3,4-

Ethylenedioxythiophene). *Nat. Mater.* **2011**, *10* (6), 429–433.

(7) Beretta, D.; Bruno, P.; Lanzani, G.; Caironi, M. Reliable Measurement of the Seebeck Coefficient of Organic and Inorganic Materials between 260 K and 460 K. *Rev. Sci. Instrum.* **2015**, *86* (7), 75104.

(8) Abadlia, L.; Gasser, F.; Khalouk, K.; Mayoufi, M.; Gasser, J. G. New Experimental Methodology, Setup and LabView Program for Accurate Absolute Thermoelectric Power and Electrical Resistivity Measurements between 25 and 1600 K: Application to Pure Copper, Platinum, Tungsten, and Nickel at Very High Temperatures. *Rev. Sci. Instrum.* **2014**, *85* (9), 95121.

(9) Schmidt, V.; Mensch, P. F. J.; Karg, S. F.; Gotsmann, B.; Das Kanungo, P.; Schmid, H.; Riel, H. Using the Seebeck Coefficient to Determine Charge Carrier Concentration, Mobility, and Relaxation Time in InAs Nanowires. *Appl. Phys. Lett.* **2014**, *104* (1), 12113.

(10) Glaudell, A. M.; Cochran, J. E.; Patel, S. N.; Chabinyc, M. L. Impact of the Doping Method on Conductivity and Thermopower in Semiconducting Polythiophenes. **2015**.